NUCL SCI TECH (2022) 33:132
https://doi.org/10.1007/s41365-022-01114-x

Non-frozen process of heavy-ion fusion reactions at deep sub-barrier energies

Kai-Xuan Cheng[1] · Jie Pu[1] · Yu-Ting Wang[1] · Ya-Fei Guo[1] · Chun-Wang Ma[1]

Received: 13 June 2022 / Revised: 24 August 2022 / Accepted: 28 August 2022 / Published online: 14 October 2022

Abstract The hindrance in heavy-ion fusion reactions at deep sub-barrier energies is investigated using the double folding model with a hybrid method between the frozen and adiabatic density approximations. In this method, the density distributions of the projectile and the target depend closely on the distance between them. As the distance decreased, the half-density radii of the colliding nuclei gradually increased to the half-density radius of the compound nucleus. The total potential based on this non-frozen approximation generates a slightly shallower pocket and becomes more attractive inside the pocket compared to that obtained from the frozen approximation. A damping factor was used to simulate the decline of the coupled channel effects owing to the density rearrangement of the two colliding nuclei. The calculated fusion cross-sections and astrophysical S factors at the deep sub-barrier energies are both in good agreement with the experimental data for the medium-heavy ^{64}Ni + ^{64}Ni and medium-light ^{24}Mg + ^{30}Si mass systems. In addition, it was concluded that the apparent maximum of the S factors most likely appears in fusion systems with strong coupling effects.

This work was supported by the National Natural Science Foundation of China (Nos. 12105080, 12105079, and 11975091) and the Program for Innovative Research Team (in Science and Technology) in University of Henan Province, China (No. 21IRTSTHN011).

✉ Kai-Xuan Cheng
chengkaixuan@htu.edu.cn

✉ Chun-Wang Ma
machunwang@126.com

[1] School of Physics, Henan Normal University, Xinxiang 453007, China

Keywords Adiabatic approximation · Double folding model · Fusion hindrance

1 Introduction

Heavy-ion fusion reactions are important for understanding the fundamental properties of quantum tunneling in complex many-body systems. As fusion occurs, the relative motion of the two colliding nuclei must overcome a Coulomb barrier, which is composed of the short-range attractive nuclear potential and the long-range repulsive Coulomb potential. When the collision energy is near or above the Coulomb barrier, a simple one-dimensional potential model sufficiently describes the fusion process. However, at energies below the Coulomb barrier, the coupling effects between the relative motion of the colliding nuclei and the nuclear intrinsic degrees of freedom, such as the vibrations and rotations of the target or projectile, play an important role in quantum tunneling [1–3]. A significant increase in fusion cross-sections at sub-barrier energies was observed compared to the results of a simple one-dimensional potential model [4–8]. Considering these coupling effects, the coupled-channel (CC) model has been successfully used in several fusion reaction calculations [9–12].

Recently, at collision energies significantly below the Coulomb barrier, an unexpected steep falloff feature of the experimental fusion cross-section, in contrast to the theoretical prediction, presents a new challenge to the current fusion theory [13–15]. This steep falloff feature in the experimental data, also called "fusion hindrance," is difficult to explain by the CC model and has gained widespread attention once again in heavy-ion fusion reactions

[16–23], especially astrophysical fusion reactions such as $^{12}C + ^{12}C$ [24–29]. The key to understanding this hindrance phenomenon is dealing with the density of the composite system after two colliding contacts. Thus far, two different assumptions have been proposed to describe the transformation from a projectile and target to a compound nucleus, namely the sudden and adiabatic approaches. Based on the sudden or frozen density approximation, it was assumed that the densities of the two colliding nuclei were frozen. Therefore, there should be a strong repulsive core in the nuclear potential of heavy-ion fusion systems in strong density overlap regions, resulting from the incompressibility properties of nuclear matter [30–32] or the Pauli exclusion principle of many-body quantum systems comprising fermions [33–36]. On the other hand, in the adiabatic approach, fusion is considered to occur slowly, thus allowing the density of the composite system to have sufficient time to rearrange. In [37, 38], Ichikawa et al. constructed an adiabatic one-body potential to describe the neck formation between two colliding nuclei in the overlap region, and a damping factor was introduced in the standard CC model to describe the physical process for the gradual transition from the sudden to adiabatic approximations. Because the assumptions employed by these two methods are completely contradictory, the depths of the potential pockets inside the Coulomb barrier significantly differ [3, 38]. In addition, as a common feature, the potentials obtained from these two methods are both wider than the commonly used Akyüz-Winther (AW) potential [39], which is successful in describing the fusion reactions above and at sub-barrier energies; however it is difficult to explain the fusion hindrance at deep sub-barrier energies [16].

As a reverse quantum tunneling process with fusion, radioactive α decay in heavy nuclei was successfully conducted by microscopic calculations, revealing significant details regarding the internal structure of nuclei [40–42]. For example, in [40], Röpke et al. concluded that owing to strong Pauli blocking effects, the α particle is highly sensitive to the surrounding matter. When approaching the nucleus ^{208}Pb, the α particle dissolves in the density overlap region and its four nucleons mix with the surrounding matter, which indicates that the α-particle size increases and the density distribution changes with a decrease in the distance between the center of mass of the α particle and the ^{208}Pb nucleus. Furthermore, to remove the sudden approximation in heavy-ion fusion reactions, Reichstein and Malik employed a special non-frozen approach to calculate the $^{16}O + ^{16}O$ potential by introducing a distance dependence to the density parameters, demonstrating a transformation from the density distributions of the reactants to that of a compound nucleus [43]. This method was also recently employed to study the elastic scattering and fusion reactions of the $^{12}C + ^{12}C$ system [44, 45]. In this study, instead of the frozen density approximation, the non-frozen approximation was employed by the double folding model to analyze the fusion process in a strong density overlap region. Considering $^{64}Ni + ^{64}Ni$ and $^{24}Mg + ^{30}Si$ fusion reactions as examples, the potentials based on the non-frozen and frozen density approximations are compared in detail. The fusion cross sections, particularly the hindrance at deep sub-barrier energies, and the astrophysical S factor were both investigated by considering this non-frozen approach.

In Sect. 2, we provide an explicit form of the double folding potential and briefly describe the non-frozen method. The differences between the frozen potential and non-frozen potential, as well as the fusion cross-sections, are presented in Sect. 3. A summary is presented in Sect. 4.

2 Theoretical framework

2.1 The coupled channel method

The CCFULL computer code was applied to calculate the fusion cross-sections [3, 11], the incoming wave boundary condition (IWBC) was imposed in the calculations, and the absorption radius was considered to be at the minimum of the potential pocket inside the Coulomb barrier. With the IWBC, the coupled-channel equations can be given by the following [3]:

$$\left[-\frac{\hbar^2}{2\mu}\frac{\mathrm{d}^2}{\mathrm{d}R^2}+\frac{J(J+1)\hbar^2}{2\mu R^2}+V(R)+\epsilon_n-E\right]u_n(R)+\sum_m V_{nm}(R)u_m(R)=0, \quad (1)$$

where E is the incident energy in the center-of-mass frame, and ϵ_n and u_n are the excitation energy and radial wave function of the nth channel, respectively. The total potential $V(R)$ between two colliding nuclei consists of the nuclear and Coulomb interactions, that is, $V(R) = V_{\mathrm{N}}(R) + V_{\mathrm{C}}(R)$. The nuclear $V_{\mathrm{N}}(R)$ and Coulomb $V_{\mathrm{C}}(R)$ interactions used in the calculations were both obtained using the double-folding procedure.

The symbol $V_{nm}(R)$ in Eq. (1) denotes the matrix of the coupling Hamiltonian, which includes both Coulomb and nuclear components. The Coulomb coupling matrix elements V^{C}_{nm} were calculated using linear coupling approximation [1, 3, 11]. The nuclear coupling Hamiltonian was generated by introducing a dynamical operator $\hat{O}_\lambda$ in the calculations, which is given by $\widetilde{V}_{\mathrm{N}}(R,\hat{O}_\lambda) = V_{\mathrm{N}}(R-\hat{O}_\lambda)$ [3, 11]. For vibrational coupling, the operator $\hat{O}_\lambda$ is given

by $\hat{O}_\lambda = (\beta^*/\sqrt{4\pi})R_i(\alpha^\dagger_{\lambda 0} + \alpha_{\lambda 0})$ [1, 3, 11], where $\alpha^\dagger_{\lambda 0}$ and $\alpha_{\lambda 0}$ are the creation and annihilation operators of the phonons, respectively, the eigenvalues λ and eigenvectors $|\alpha\rangle$ of the operator $\hat{O}$ satisfy $\hat{O}_\lambda|\alpha\rangle = \lambda_\alpha|\alpha\rangle$, R_i is the radius of the projectile or target, and β^* denotes the corresponding deformation parameter. The nuclear coupling matrix elements were then evaluated using [3]

$$\begin{aligned} V^{\mathrm{N}}_{nm} &= \langle n|\widetilde{V}_{\mathrm{N}}(R,\hat{O}_\lambda)|m\rangle - V_{\mathrm{N}}(R)\delta_{n,m} \\ &= \sum_\alpha \langle n|\alpha\rangle\langle\alpha|m\rangle \widetilde{V}_{\mathrm{N}}(R,\lambda_\alpha) - V_{\mathrm{N}}(R)\delta_{n,m}. \end{aligned} \tag{2}$$

The nuclear coupling potential $\widetilde{V}_{\mathrm{N}}(R,\lambda_\alpha) = V_{\mathrm{N}}(R-\lambda_\alpha)$ is taken up to the second order of λ_α [1, 3, 11]

$$\widetilde{V}_{\mathrm{N}}(R,\lambda_\alpha) = V_{\mathrm{N}}(R) - \frac{\mathrm{d}V_{\mathrm{N}}(R)}{\mathrm{d}R}\lambda_\alpha + \frac{1}{2}\frac{\mathrm{d}^2V_{\mathrm{N}}(R)}{\mathrm{d}R^2}\lambda^2_\alpha, \tag{3}$$

where the first term $V_{\mathrm{N}}(R)$ is the nuclear potential in the absence of coupling, and the second and third terms are the nuclear coupling form factors, which are closely associated with the nuclear potential.

The penetrability P_J can be obtained by solving the CC equations, and the total fusion cross-section σ_{fus} is then obtained by summing the partial fusion cross-section [3]:

$$\sigma_{\mathrm{fus}}(E) = \frac{\pi}{k^2}\sum_J (2J+1)P_J(E), \tag{4}$$

where $k = \sqrt{2\mu E/\hbar^2}$ is the wave number associated with energy E.

2.2 The double folding potential

The explicit form of the potential between the projectile and target nuclei is presented herein. The double-folding model was used to calculate the nucleus-nucleus potential. This model has been widely used to analyze the elastic and inelastic scattering of heavy ions [46, 47]. However, it is difficult to explain the fusion process in a strong-density overlap region [48]. When the projectile and target nuclei start touching one another, the Pauli blocking effects become increasingly important owing to the density overlap. Considering the Pauli blocking potential resulting from the antisymmetrization, a modified double-folding potential was employed to analyze the heavy-ion fusion processes as follows [21]:

$$\begin{aligned} V_{\mathrm{N}}(\mathbf{R}) &= V_{\mathrm{D}}(\mathbf{R}) + V_{\mathrm{P}}(\mathbf{R}) \\ &= \int \mathrm{d}\mathbf{r_1}\mathrm{d}\mathbf{r_2}\rho_{\mathrm{p}}(\mathbf{r_1})\rho_{\mathrm{t}}(\mathbf{r_2})g(|\mathbf{s_1}|) \\ &\quad + \int \mathrm{d}\mathbf{r_1}\rho_{\mathrm{p}}(\mathbf{r_1})v(|\mathbf{s_2}|), \end{aligned} \tag{5}$$

$$g(|\mathbf{s_1}|) = 9846\frac{\exp(-4s_1)}{4s_1} - 3139\frac{\exp(-2.5s_1)}{2.5s_1}, \tag{6}$$

$$v(|\mathbf{s_2}|) = 437.05\rho_{\mathrm{t}}(s_2) + 983.89\rho^2_{\mathrm{t}}(s_2). \tag{7}$$

where $g(|\mathbf{s_1} = \mathbf{R} - \mathbf{r_1} + \mathbf{r_2}|)$ denotes the direct interaction between a nucleon in the target nucleus and a nucleon in the projectile nuclei, and $v(|\mathbf{s_2} = \mathbf{R} - \mathbf{r_1}|)$ denotes the Pauli blocking interaction of a single nucleon in the projectile nuclei from the target density. ρ_{p} and ρ_{t} denote the density distributions of the projectile and target nuclei, respectively. This nuclear potential, including the Pauli blocking effect, has been successful in applying the fusion processes of 95 systems and has significantly improved the explanation of fusion cross-sections at deep sub-barrier energies [21]. The Coulomb potential employed in the calculations was the double-folding integral of the proton-proton Coulomb interaction:

$$V_{\mathrm{C}}(\mathbf{R}) = \int \mathrm{d}\mathbf{r_1}\mathrm{d}\mathbf{r_2}\frac{e^2}{|\mathbf{s_1}|}\rho_{\mathrm{pp}}(\mathbf{r_1})\rho_{\mathrm{tp}}(\mathbf{r_2}), \tag{8}$$

where ρ_{pp} and ρ_{tp} are the proton density distributions of the projectile and target nuclei, respectively, and e is the elementary charge.

The density distributions of the projectile and target nuclei are usually parameterized with Fermi–Dirac distribution functions [49]:

$$\rho_i(r) = \frac{\rho_{0i}}{1+\exp\left(\frac{r-C_i}{a_i}\right)}, \tag{9}$$

where ρ_i, C_i, and a_i indicate the density, half-density radius, and diffuseness of the neutrons ($i = \mathrm{n}$) and protons ($i = \mathrm{p}$), respectively. ρ_{0i} is obtained by integrating the matter density distribution that is equivalent to the neutron or proton numbers. In the sudden or frozen density approximation (FDA), the densities of the two colliding nuclei are assumed to be frozen for simplicity, that is, the parameters of ρ_{i0}, C_i, and a_i in Eq. (9) are fixed during the fusion process.

2.3 The non-frozen density approximation

In the adiabatic model, the fusion reaction is assumed to occur slowly, thus the density distribution has sufficient time to adjust to the optimized distribution [3]. To describe the adiabatic picture, several different methods were employed to determine the transformation process of the density distribution and obtain the adiabatic potential after the overlap of the two colliding nuclei [38, 43, 50, 51]. In [43], Reichstein and Malik introduced a special nonfrozen density approximation (NFDA), the ^{16}O + ^{16}O fusion reaction. A similar approach was recently successfully employed to describe the elastic scattering and fusion data

for the $^{12}C + ^{12}C$ reaction [44, 45]. This approach introduces the distance dependence R to the density parameters C and a as follows:

$$C(R) = \begin{cases} C, & R > R_c \\ C_{cn} \exp\left[\ln\left(\frac{C}{C_{cn}}\right) \cdot \frac{R^2}{R_c^2}\right], & R \le R_c \end{cases} \quad (10)$$

and the same hypothesis for the diffuseness parameter a. Here, C_{cn} is the half-density radius of the compound nucleus and R_c is the distance between the projectile and target, where the density of the overlap region is the central density of the compound nuclei. At the beginning of the density overlap or before approaching the distance R_c, the density distribution of the two colliding nuclei can be considered frozen. In the strong density overlap region, namely $R \le R_c$, there is a density transformation from two colliding nuclei to a compound nucleus.

Considering this non-frozen process, the standard CC framework is necessary to modify it by introducing a damping factor that describes the physical process for transitioning from the sudden to adiabatic approximations [37, 38]. To avoid the double counting of the CC effects, we introduced the following damping factor to simulate the decrease in the excitation strengths of the colliding nuclei, such as the vibrational states [38]:

$$\Phi(R, \lambda_\alpha) = \begin{cases} \exp\left[-(R - R_d - \lambda_\alpha)^2 / 2a_d^2\right], & R \le R_d + \lambda_\alpha, \\ 1, & R > R_d + \lambda_\alpha, \end{cases} \quad (11)$$

where R_d and a_d are parameters indicating the damping radius and diffuseness, respectively. Instead of Eq. (3) in the CC model, the nuclear coupling potential was employed [37, 38]:

$$\widetilde{V}_N(R, \lambda_\alpha) = V_N(R) - \left[\frac{dV_N(R)}{dR}\lambda_\alpha + \frac{1}{2}\frac{d^2V_N(R)}{dR^2}\lambda_\alpha^2\right]\Phi(R, \lambda_\alpha). \quad (12)$$

The CC equation performed sufficiently at large distances. With a decrease in distance, the non-frozen process gradually plays a leading role, and the CC model is close to the one-dimensional potential model.

3 Results and discussions

Considering the medium-heavy mass system of $^{64}Ni + ^{64}Ni$ and medium-light mass system of $^{24}Mg + ^{30}Si$ as examples, the potentials and fusion cross-sections obtained by the aforementioned non-frozen process are discussed in the following sections. Before presenting the detailed theoretical results, we clarify the parameters used in the calculations. The densities used to calculate the double-folding potential are listed in Table 1. The input parameters for the coupling strengths in the CC calculations for $^{64}Ni + ^{64}Ni$ and $^{24}Mg + ^{30}Si$ systems were obtained from Ref. [38] and are tabulated in Table 2. The damping radius R_d and diffuseness a_d parameters used in Eq. (11) are 1.298 fm and 1.25 fm for the $^{64}Ni + ^{64}Ni$ fusion system, and 1.430 fm and 1.25 fm for the $^{24}Mg + ^{30}Si$ fusion system [38].

3.1 The medium-heavy mass system $^{64}Ni + ^{64}Ni$

First, the density distribution of the FDA and NFDA after two colliding nuclei overlap is presented in Fig. 1. Based on the FDA, the densities of the two colliding nuclei are independent of the distance R and are fixed. However, the NFDA describes a density transformation from the colliding nuclei to the compound nucleus. Before distance R_c, the two colliding nuclei maintain their individuality. After reaching R_c, the half-density radii C of the projectile and target begin to increase, and the nucleons in the center region of the projectile and target gradually diffuse to the edge, that is, the compact nuclei dissolve. According to the normalization condition, the central densities of the projectile and target nuclei decreased, and their surface densities increased. For the $^{64}Ni + ^{64}Ni$ system, before the distance reached $R_c = 8.6$ fm, the overlap density distributions obtained from the FDA and NFDA were the same, as indicated by the dashed lines in Fig. 1. At $R = 6.5$ fm, the two results indicate that the fusion processes at small distances are different and the density distribution of the NFDA is looser. Note, at the initial stage of density rearrangement (8.0 fm $\le R < 8.6$ fm), the density overlap region is mainly contributed by the colliding nuclei in the diffuseness region. Therefore, the density at $Z = 0$ fm

Table 1 Parameters of the density distribution for ^{24}Mg, ^{30}Si, ^{54}Fe, ^{64}Ni, and ^{128}Ba nuclei

Nucleus	C_p	a_p	C_n	a_n	References
^{24}Mg	3.032	0.52	3.032	0.52	[52]
^{30}Si	3.130	0.48	3.130	0.48	[52]
^{54}Fe	4.134	0.51	4.058	0.52	[53]
^{64}Ni	4.260	0.58	4.340	0.53	[31]
^{128}Ba	5.580	0.50	5.570	0.53	[53]

C_i (fm) and a_i (fm) are the half-density radius and diffuseness of the neutron ($i = n$) and proton ($i = p$) used in Eq. (9). The last column presents the corresponding references where the parameters were obtained from

Table 2 Parameters used in the CC calculations

Nucleus	λ^{π}	E_{ex} (MeV)	β^{c}	β^{n}	N_{ph}
^{24}Mg	2^{+}	1.369	0.608	0.460	1
^{30}Si	2^{+}	2.235	0.330	0.330	1
	3^{-}	5.497	0.275	0.275	1
^{64}Ni	2^{+}	1.346	0.165	0.185	2
	3^{-}	3.560	0.193	0.200	1

λ^{π} denotes the multipolarity and parity of a state. E_{ex} denotes the excitation energy of a state. β^{c} and β^{n} denote the deformation parameters for the Coulomb and nuclear coupling strengths, respectively. N_{ph} in the last column indicates the number of phonons included in the calculations

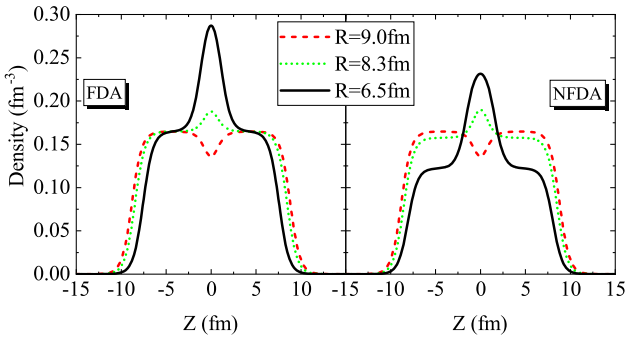

Fig. 1 (Color online) Comparison of the overlap density distribution obtained from the FDA and NFDA at the varying distance R for the ^{64}Ni + ^{64}Ni fusion system. The distance R_c used in Eq. (10) is 8.6 fm, where the density of the overlap region is equal to the central density of the compound nuclei ^{128}Ba

obtained from the NFDA was slightly higher than that obtained from the FDA; as shown in Fig. 1, at a distance R = 8.3 fm, the maximum density of NFDA was 0.1900 fm^{-3} and only 0.1880 fm^{-3} for FDA. This slight difference that results from the surface density rearrangement has a significant influence on the nucleus-nucleus potential presented below.

Here, we provide a detailed comparison of the potentials demonstrated in Fig. 2 for the ^{64}Ni + ^{64}Ni fusion system. Before reaching a distance of 8.6 fm, the potentials obtained from the FDA and NFDA were the same, and the difference became increasingly apparent as the distance R decreased. At the initial stage of the density rearrangement, the surface density rearrangement indicated above leads to the potential of the NFDA being more repulsive for the Pauli blocking term and more attractive for the direct term compared to the FDA results, as shown in Fig. 2a and b. However, as the nuclei become distant, the Pauli blocking potential and the direct potential obtained from the NFDA have weaker effects, corresponding to a weaker density overlap. As the sum of V_P and V_D, the nuclear potential V_N shown in Fig. 2c resulted from the NFDA becoming more attractive at a small radii compared to the result of the FDA. As shown in Fig. 2d, the long-range Coulomb potential, which is not affected by this surface density rearrangement, is always less repulsive by considering the NFDA.

The total potentials and fusion cross-sections are shown in Fig. 3. The commonly used potentials in heavy-ion fusion reactions, such as the Akyüz-Winther (AW) potential [39], are also presented in Fig. 3a for comparison. Two double folding potentials, namely FDA and NFDA, exhibit similar behavior to the AW potential outside the Coulomb barrier and generate shallow pockets inside the Coulomb barrier owing to the Pauli blocking effect. The two potentials obtained from the FDA and NFDA are distinguished after two colliding nuclei approach the distance R = 8.6 fm, where the density distributions of the colliding nuclei begin to change. At the initial stage of the density rearrangement, the stronger density overlap of NFDA resulted in a slightly shallower pocket than that of FDA. With a decrease in the distance R, the two potentials demonstrated apparently different energy dependencies, and the NFDA became more attractive. However, this difference between the two potentials inside the pocket does not contribute to the calculated fusion cross-sections owing to the IWBC adopted in the heavy-ion fusion model.

In Fig. 3b, the calculated fusion cross sections based on the CC model are compared with the experimental data [54]. The experimental fusion cross-sections near the Coulomb barrier energies are underestimated by the no-coupling results (thin solid line) and are sufficiently described by considering the CC effect. As the collision energies decrease to deep sub-barrier energies, the experimental data exhibit a strong suppression compared to the AW results (dotted line). This phenomenon is referred to as fusion hindrance and mainly results from the density overlap in the fusion process. Although the fusion cross sections calculated by FDA, which include the Pauli blocking potential, present a significant improvement, it remains difficult for the astrophysical S factor obtained from the FDA to represent the experimental maximum at deep sub-barrier energies, as shown in the insert of Fig. 3b. Considering the similar behavior of the FDA and NFDA potential outside the pocket, there was no apparent difference between the fusion cross-sections of the FDA and NFDA. However, considering the damping effect of the CC framework resulting from the density arrangement, the calculated fusion cross sections presented a steep falloff at deep sub-barrier energies, sufficiently presenting the experimental data. Importantly, the S factor obtained from the NFDA with the damping factor ceases to increase and appears to be maximum at deep sub-barrier energies.

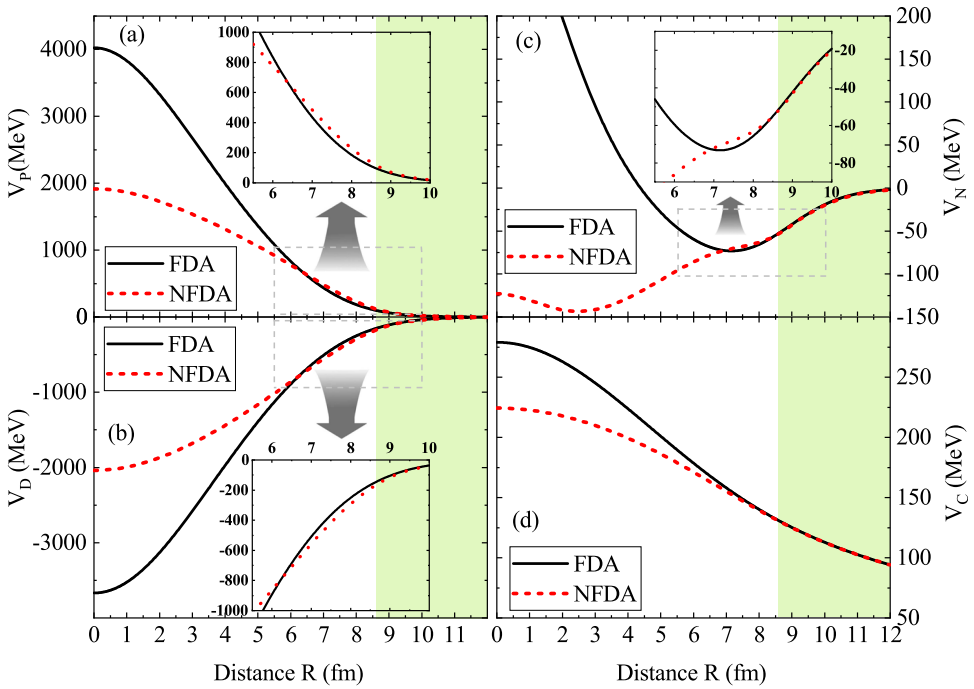

Fig. 2 (Color online) Comparison of the potential obtained from FDA (solid line) and NFDA (dashed line) for the ^{64}Ni + ^{64}Ni fusion system. **a**, **b**, and **c** present the Pauli blocking term V_P, direct term V_D, and the nuclear interaction V_N in Eq. (5), respectively. **d** Presents the Coulomb interaction V_C in Eq. (8). The shadow zone denotes the area of distance $R >$ 8.6 fm

3.2 The medium-light mass system ^{24}Mg + ^{30}Si

Fig. 4 presents the obtained total potential and fusion cross sections for the medium-light mass system ^{24}Mg + ^{30}Si. Similar to the ^{64}Ni + ^{64}Ni fusion system, considering the non-frozen process, the potential from colliding nuclei to the compound nucleus, namely the NFDA, also presented a slightly shallower pocket compared to the result of FDA shown in Fig. 4a. The fusion cross-sections obtained from the FDA and NFDA with or without the damping factor sufficiently explain the fusion hindrance to a certain extent, as shown in Fig. 4b. By introducing the damping factor, the fusion cross-sections of the NFDA presented a stronger energy dependence at deep sub-barrier energies and then rapidly converged to the results indicating no coupling. The S factors calculated by the FDA and NFDA, with or without the damping factor, were all in good agreement with the experimental data. Although the growth of the slope for the S factor slowed with decreasing energies, the maximum of the S factor calculated by NFDA with the damping factor is not visible in the insert shown in Fig. 4b.

In comparison with the medium-light mass system ^{24}Mg + ^{30}Si, the density rearrangement of the ^{64}Ni + ^{64}Ni system in the overlap region has a significant impact on the fusion and presents a relatively apparent damping effect of the CC strength. The S factor calculated with the damping factor ceases to increase and exhibits a maximum at deep sub-barrier energies in the ^{64}Ni + ^{64}Ni fusion system. However, in the relatively light mass system ^{24}Mg + ^{30}Si, the growth of the S factor at lower energies was slowed by considering the non-frozen condition with a relatively weak damping effect. This difference in the behavior of the S factor may provide a valuable reference for the currently controversial fusion process of ^{12}C + ^{12}C at low energies, which strongly affects the estimation of astrophysical reaction rates.

4 Summary

The fusion hindrance phenomenon observed at deep sub-barrier energies was investigated using a double folding model based on the non-frozen density approximation. In this non-frozen method, the density distribution transformation from the projectile and target nuclei to the compound nucleus is described by introducing the distance dependence to the half-density radius and diffuseness parameters. When the density of the overlapping region reaches the central density of the compound nuclei, the projectile and target density distributions begin to change. The enlarged half-density radius reduces the central density of the colliding nucleus according to the normalization condition. At the initial stage of the density rearrangement, the increasing surface density of the colliding nuclei plays a dominant role in the overlapping region. The slightly higher overlap density of the non-frozen process causes the potential to have a shallower pocket compared to that of the frozen potential. As the distance decreases, the non-frozen fusion process exhibits a relatively weak density

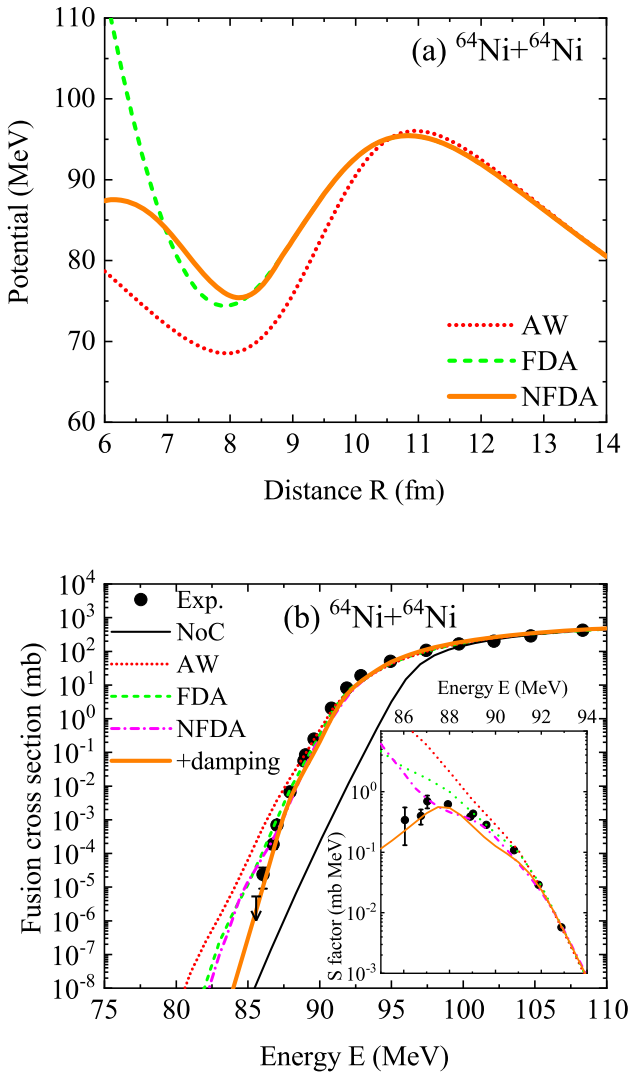

Fig. 3 (Color online) **a** Comparison of the total potentials obtained from AW (dotted line), FDA (dashed line), and NFDA (solid line) for the ^{64}Ni + ^{64}Ni fusion system. **b** The experimental fusion cross sections for the ^{64}Ni + ^{64}Ni [54] fusion system compared to the theoretical calculation results. The dotted and dashed lines denote the results of the AW and FDA potentials. The results calculated by the NFDA potential with and without the damping factor are displayed by the dash-dotted and solid lines, respectively. The insert presents a comparison of the S factors between the experimental data and calculated results

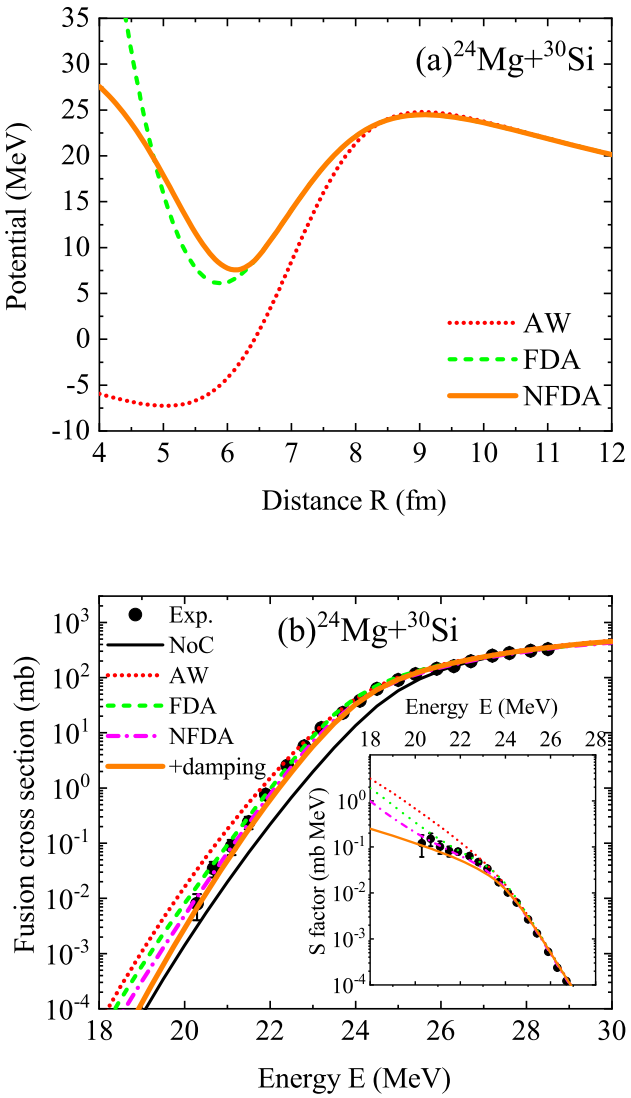

Fig. 4 (Color online) Same as Fig. 3, but for the fusion system ^{24}Mg + ^{30}Si. The solid points indicate the experimental data obtained from Refs. [52, 55]

overlap, and the corresponding potential is significantly more attractive than the frozen potential.

The CC effects have a significant influence on heavy ion fusion reactions. In the non-frozen picture, the CC effects decrease owing to the density rearrangement, and a damping factor is employed to simulate this process. Based on the non-frozen approximation with the damping factor, the calculated fusion cross sections and astrophysical S factors for ^{64}Ni + ^{64}Ni and ^{24}Mg + ^{30}Si are both in good agreement with the experimental data. For a relatively heavy mass fusion system, such as the ^{64}Ni + ^{64}Ni reaction, the non-frozen process with the damping of the CC strength causes a drastic reduction in the fusion cross section, and a clear maximum is exhibited in the astrophysical S factor. In the medium-light mass system ^{24}Mg + ^{30}Si, the damping effect is relatively weak, and the predicted S factor demonstrates that there is no maximum at low collision energies.

It would be noteworthy to extend this method to astrophysical fusion systems, such as the ^{12}C + ^{12}C reaction. For the ^{12}C + ^{12}C fusion reaction at low energies, the fusion process can be considered a superposition of the non-resonant background and an additional contribution of resonance [56–59]. This method can be helpful in

understanding the fusion process of non-resonant effects at astrophysical energies for $^{12}C + ^{12}C$ reactions.

Author Contributions All authors contributed to the study conception and design. Material preparation, data collection and analysis were performed by Kai-Xuan Cheng, Jie Pu and Chun-Wang Ma. The first draft of the manuscript was written by Kai-Xuan Cheng, and all authors commented on previous versions of the manuscript. All authors read and approved the final manuscript.

References

1. H. Esbensen, S. Landowne, Higher-order coupling effects in low energy heavy-ion fusion reactions. Phys. Rev. C **35**, 2090 (1987). https://doi.org/10.1103/PhysRevC.35.2090
2. A.B. Balantekin, N. Takigawa, Quantum tunneling in nuclear fusion. Rev. Mod. Phys. **70**, 77 (1998). https://doi.org/10.1103/RevModPhys.70.77
3. K. Hagino, N. Takigawa, Subbarrier fusion reactions and many-particle quantum tunneling. Prog. Theor. Phys. **128**, 1061 (2012). https://doi.org/10.1143/PTP.128.1061
4. J.O. Newton, C.R. Morton, M. Dasgupta et al., Experimental barrier distributions for the fusion of ^{12}C, ^{16}O, ^{28}Si, and ^{35}Cl with ^{92}Zr and coupled-channels analyses. Phys. Rev. C **64**, 064608 (2001). https://doi.org/10.1103/PhysRevC.64.064608
5. K. Hagino, N. Takigawa, M. Dasgupta et al., Validity of the linear coupling approximation in heavy-ion fusion reactions at sub-barrier energies. Phys. Rev. C **55**, 276 (1997). https://doi.org/10.1103/PhysRevC.55.276
6. C.J. Lin, H.M. Jia, H.Q. Zhang et al., Systematic study of the surface properties of the nuclear potential with high precision large-angle quasi-elastic scatterings. Phys. Rev. C **79**, 064603 (2009). https://doi.org/10.1103/PhysRevC.79.064603
7. F. Niu, P.-H. Chen, H.-G. Cheng et al., Multinucleon transfer dynamics in nearly symmetric nuclear reactions. Nucl. Sci. Tech. **31**, 59 (2020). https://doi.org/10.1007/s41365-020-00770-1
8. P.-H. Chen, F. Niu, Y.-F. Guo, Z.-Q. Feng, Nuclear dynamics in multinucleon transfer reactions near Coulomb barrier energies. Nucl. Sci. Tech. **29**, 185 (2018). https://doi.org/10.1007/s41365-018-0521-y
9. C.H. Dasso, S. Landowne, CCFUS—a simplified coupled-channel code for calculation of fusion cross sections in heavy-ion reactions. Comput. Phys. Commun. **46**, 187 (1987). https://doi.org/10.1016/0010-4655(87)90045-2
10. J. Fernández-Niello, C.H. Dasso, S. Landowne, CCDEF-a simplified coupled-channel code for fusion cross sections including static nuclear deformations. Comput. Phys. Commun. **54**, 409 (1989). https://doi.org/10.1016/0010-4655(89)90100-8
11. K. Hagino, N. Rowley, A.T. Kruppa, A program for coupled-channel calculations with all order couplings for heavy-ion fusion reactions. Comput. Phys. Commun. **123**, 143 (1999). https://doi.org/10.1016/S0010-4655(99)00243-X
12. M. Hosamani, A. Vinayak, N. Badiger, Investigating the effect of entrance channel mass asymmetry on fusion reactions using the Skyrme energy density formalism. Nucl. Sci. Tech. **31**, 89 (2020). https://doi.org/10.1007/s41365-020-00802-w
13. C.L. Jiang, H. Esbensen, K.E. Rehm et al., Unexpected behavior of heavy-Ion fusion cross sections at extreme sub-barrier energies. Phys. Rev. Lett. **89**, 052701 (2002). https://doi.org/10.1103/PhysRevLett.89.052701
14. B.B. Back, H. Esbensen, C.L. Jiang et al., Recent developments in heavy-ion fusion reactions. Rev. Mod. Phys. **86**, 317 (2014). https://doi.org/10.1103/RevModPhys.86.317
15. M. Dasgupta, D.J. Hinde, A. Diaz-Torres et al., Beyond the coherent coupled channels description of nuclear fusion. Phys. Rev. Lett. **99**, 192701 (2007). https://doi.org/10.1103/PhysRevLett.99.192701
16. K. Hagino, N. Rowley, M. Dasgupta, Fusion cross sections at deep sub-barrier energies. Phys. Rev. C **67**, 054603 (2003). https://doi.org/10.1103/PhysRevC.67.054603
17. V.V. Sargsyan, Z. Kanokov, G.G. Adamian et al., Capture process in nuclear reactions with a quantum master equation. Phys. Rev. C **80**, 034606 (2009). https://doi.org/10.1103/PhysRevC.80.034606
18. V. Yu Denisov, Nucleus-nucleus potential with shell-correction contribution. Phys. Rev. C **91**, 024603 (2015). https://doi.org/10.1103/PhysRevC.91.024603
19. C.L. Jiang, B.B. Back, K.E. Rehm et al., Heavy-ion fusion reactions at extreme subbarrier energies. Eur. Phys. J. A **57**, 235 (2021). https://doi.org/10.1140/epja/s10050-021-00536-2
20. VYu. Denisov, Multidimensional harmonic oscillator model of subbarrier fusion. Eur. Phys. J. A **58**, 91 (2022). https://doi.org/10.1140/epja/s10050-022-00746-2
21. K.-X. Cheng, C. Xu, C.-W. Ma et al., Pauli blocking potential applied to heavy-ion fusion reactions. Chin. Phys. C **46**, 024105 (2022). https://doi.org/10.1088/1674-1137/ac3749
22. D. Boilley, B. Cauchois, H.L. Lü et al., How accurately can we predict synthesis cross sections of superheavy elements? Nucl. Sci. Tech. **29**, 172 (2018). https://doi.org/10.1007/s41365-018-0509-7
23. Z.-Q. Feng, Nuclear dynamics and particle production near threshold energies in heavy-ion collisions. Nucl. Sci. Tech. **29**, 40 (2018). https://doi.org/10.1007/s41365-018-0379-z
24. C.L. Jiang, B.B. Back, H. Esbensen et al., Origin and consequences of $^{12}C + ^{12}C$ fusion resonances at deep sub-barrier energies. Phys. Rev. Lett. **110**, 072701 (2013). https://doi.org/10.1103/PhysRevLett.110.072701
25. C.L. Jiang, D. Santiago-Gonzalez, S. Almaraz-Calderon et al., Reaction rate for carbon burning in massive stars. Phys. Rev. C **97**, 012801(R) (2018). https://doi.org/10.1103/PhysRevC.97.012801
26. N.T. Zhang, X.Y. Wang, D. Tudor et al., Constraining the $^{12}C + ^{12}C$ astrophysical S-factors with the $^{12}C + ^{13}C$ measurements at very low energies. Phys. Lett. B **801**, 135170 (2020). https://doi.org/10.1016/j.physletb.2019.135170
27. T.-P. Luo, P.-W. Wen, C.-J. Lin et al., Bayesian analysis on non-resonant behavior of $^{12}C + ^{12}C$ fusion reaction at sub-barrier energies. Chin. Phys. C **46**, 064105 (2022). https://doi.org/10.1088/1674-1137/ac5587
28. V.V. Sargyan, G.G. Adamian, N.V. Antonenko, H. Lenske, Constraints on the appearance of a maximum in astrophysical S-factor. Phys. Lett. B **824**, 136792 (2022). https://doi.org/10.1016/j.physletb.2021.136792
29. X.-D. Tang, S.-B. Ma, X. Fang et al., An efficient method for mapping the $^{12}C+^{12}C$ molecular resonances at low energies. Nucl. Sci. Tech. **30**, 126 (2019). https://doi.org/10.1007/s41365-019-0652-9
30. Ş Mişicu, H. Esbensen, Hindrance of heavy-ion fusion due to nuclear incompressibility. Phys. Rev. Lett. **96**, 112701 (2006). https://doi.org/10.1103/PhysRevLett.96.112701
31. Ş Mişicu, H. Esbensen, Signature of shallow potentials in deep sub-barrier fusion reactions. Phys. Rev. C **75**, 034606 (2007). https://doi.org/10.1103/PhysRevC.75.034606

32. H. Esbensen, Ş Mişicu, Hindrance of $^{16}O + ^{208}Pb$ fusion at extreme subbarrier energies. Phys. Rev. C **76**, 054609 (2007). https://doi.org/10.1103/PhysRevC.76.054609
33. C. Simenel, A.S. Umar, K. Godbey et al., How the Pauli exclusion principle affects fusion of atomic nuclei. Phys. Rev. C **95**, 031601(R) (2017). https://doi.org/10.1103/PhysRevC.95.031601
34. A.S. Umar, C. Simennel, K. Godbey, Pauli energy contribution to the nucleus-nucleus interaction. Phys. Rev. C **104**, 034619 (2021). https://doi.org/10.1103/PhysRevC.104.034619
35. K.X. Cheng, C. Xu, Pauli blocking effects in α-induced fusion reactions. Phys. Rev. C **99**, 014607 (2019). https://doi.org/10.1103/PhysRevC.99.014607
36. K.X. Cheng, C. Xu, Pauli blocking effects in *n*α-nucleus-induced fusion reactions. Phys. Rev. C **102**, 014619 (2020). https://doi.org/10.1103/PhysRevC.102.014619
37. T. Ichikawa, K. Hagino, A. Iwamoto, Signature of smooth transition from sudden to adiabatic states in heavy-ion fusion reactions at deep sub-barrier energies. Phys. Rev. Lett. **103**, 202701 (2009). https://doi.org/10.1103/PhysRevLett.103.202701
38. T. Ichikawa, Systematic investigations of deep sub-barrier fusion reactions using an adiabatic approach. Phys. Rev. C **92**, 064604 (2015). https://doi.org/10.1103/PhysRevC.92.064604
39. A. Winther, Dissipation, polarization and fluctuation in grazing heavy-ion collisions and the boundary to the chaotic regime. Nucl. Phys. A **594**, 203 (1995). https://doi.org/10.1016/0375-9474(95)00374-A
40. G. Röpke, P. Schuck, Y. Funaki et al., Nuclear clusters bound to doubly magic nuclei: The case of^{212}Po. Phys. Rev. C **90**, 034304 (2014). https://doi.org/10.1103/PhysRevC.90.034304
41. C. Xu, G. Röpke, P. Schuck et al., α-cluster formation and decay in the quartetting wave function approach. Phys. Rev. C **95**, 061306(R) (2017). https://doi.org/10.1103/PhysRevC.95.061306
42. S. Yang, C. Xu, G. Röpke et al., α decay to a doubly magic core in the quartetting wave function approach. Phys. Rev. C **101**, 024316 (2020). https://doi.org/10.1103/PhysRevC.101.024316
43. I. Reichstein, F.B. Malik, Dependence of ^{16}O–^{16}O potential on the density ansatz. Phys. Lett. B **37**, 344 (1971). https://doi.org/10.1016/0370-2693(71)90197-3
44. L.H. Chien, D.T. Khoa, D.C. Cuong et al., Consistent mean-field description of the $^{12}C + ^{12}C$ optical potential at low energies and the astrophysical S factor. Phys. Rev. C **98**, 064604 (2018). https://doi.org/10.1103/PhysRevC.98.064604
45. D.T. Khoa, L.H. Chien, D.C. Cuong et al., Mean-field description of heavy-ion scattering at low energies and fusion. Nucl. Sci. Tech. **29**, 183 (2018). https://doi.org/10.1007/s41365-018-0517-7
46. G.R. Satchler, W.G. Love, Folding model potentials from realistic interactions for heavy-ion scattering. Phys. Rep. **55**, 183 (1979). https://doi.org/10.1016/0370-1573(79)90081-4
47. D.T. Khoa, α-nucleus optical potential in the double-folding model. Phys. Rev. C **63**, 034007 (2001). https://doi.org/10.1103/PhysRevC.63.034007
48. I.I. Gontcher, D.J. Hinde, M. Dasgupta et al., Double folding nucleus-nucleus potential applied to heavy-ion fusion reactions. Phys. Rev. C **69**, 024610 (2004). https://doi.org/10.1103/PhysRevC.69.024610
49. A. Bohr, B.R. Mottelson, *Nuclear Structure*, vol. 1 (World Scientific, Singapore, 1988)
50. VYu. Denisov, Multidimensional model of cluster radioactivity. Phys. Rev. C **88**, 044608 (2013). https://doi.org/10.1103/PhysRevC.88.044608
51. VYu. Denisov, Nucleus-nucleus potential with shell correction contribution and deep sub-barrier fusion of heavy nuclei. Phys. Rev. C **89**, 044604 (2014). https://doi.org/10.1103/PhysRevC.89.044604
52. C.L. Jiang, A.M. Stefanini, H. Esbensen et al., Fusion hindrance for a positive-Q-value system $^{24}Mg + ^{30}Si$. Phys. Rev. Lett. **113**, 022701 (2014). https://doi.org/10.1103/PhysRevLett.113.022701
53. W.M. Seif, H. Mansour, Systematics of nucleon density distributions and neutron skin of nuclei. Int. J. Mod. Phys. E **24**, 1550083 (2015). https://doi.org/10.1142/S0218301315500834
54. C.L. Jiang, K.E. Rehm, R.V.F. Janssens et al., Influence of nuclear structure on sub-barrier hindrance in Ni + Ni fusion. Phys. Rev. Lett. **93**, 012701 (2004). https://doi.org/10.1103/PhysRevLett.93.012701
55. A. Morsad, J.J. Kolata, R.J. Tighe et al., Sub-barrier fusion of^{28,30}Si with ^{24,26}Mg. Phys. Rev. C **41**, 988 (1990). https://doi.org/10.1103/PhysRevC.41.988
56. E.F. Aguilera, P. Rosales, E. Martinez-Quiroz et al., New γ-ray measurements for $^{12}C + ^{12}C$ sub-Coulomb fusion: toward data unification. Phys. Rev. C **73**, 064601 (2006). https://doi.org/10.1103/PhysRevC.73.064601
57. R.L. Cooper, A.W. Steiner, E.F. Brown, Possible resonances in the $^{12}C + ^{12}C$ fusion rate and superburst ignition. Astrophys. J. **702**, 660 (2009). https://doi.org/10.1088/0004-637X/702/1/660
58. A. Tumino, C. Spitaleri, M. La Cognata et al., An increase in the $^{12}C + ^{12}C$ fusion rate from resonances at astrophysical energies. Nature **557**, 687 (2018). https://doi.org/10.1038/s41586-018-0149-4
59. Y. Taniguchi, M. Kimura, $^{12}C + ^{12}C$ fusion S-factor from a full-microscopic nuclear model. Phys. Lett. B **823**, 136790 (2021). https://doi.org/10.1016/j.physletb.2021.136790